Large Rashba parameter for $4d$ strongly correlated perovskite oxide SrNbO$_3$ ultrathin films

Hikaru Okuma [*], Yumiko Katayama, and Kazunori Ueno
Department of Basic Science, The University of Tokyo, Meguro, Tokyo 153-8902, Japan

To elucidate the spin relaxation mechanism of SrNbO$_3$ (SNO) ultrathin films, the transport properties of a series of SNO films with various thicknesses t were measured on both sides of the metal-insulator transition. The spin-orbit scattering time (τ_{so}) was deduced from the analysis of the magnetoresistance with weak antilocalization theory, and it was found that τ_{so} was inversely proportional to the momentum scattering time. This result was explained in terms of the D'Yakonov-Perel mechanism, indicative of the dominant Rashba effect. The values of the Rashba parameter, on the order of 1×10^{-12} eV m were the largest in the values reported for other ultrathin films of metallic oxides.

I. INTRODUCTION

Electron systems lacking inversion symmetry show Rashba-type spin-orbit coupling (SOC) [1,2]. Heterointerfaces with large Rashba SOCs [2–5] have attracted considerable attention due to their potential spintronics applications and intriguing phenomena, such as the intrinsic spin Hall effect [6]. For spintronics, semiconductor heterointerfaces with large Rashba SOCs have been used to control spin precession in spin field effect transistors [7,8]. Recently, a remarkably high spin-to-charge conversion rate [9] was reported for an oxide heterointerface with a large Rashba SOC, which is much larger than those of other Rashba systems, such as an interface between Ag and Bi (Ag/Bi) [10], a surface of a topological insulator α-Sn [11], and heavy metals [12]. Among all systems with Rashba SOCs, oxide materials were air-stable and easy to fabricate, but their Rashba parameters α_R were smaller than those of other systems with heavy elements. There has been a lot of effort spent finding oxide semiconductor heterostructures with large α_R, such as SrTiO$_3$ (STO) [13–15] and KTaO$_3$ (KTO) [16,17] based interfaces, all of which use high mobility oxide semiconductors STO or KTO. Furthermore, there have been several reports on α_R for metallic oxide ultrathin films, such as SrIrO$_3$ (SIO) [18] and La$_{2/3}$Sr$_{1/3}$MnO$_3$ (LSMO) [19], although α_R was even smaller for these materials than for semiconductor heterostructures. Ultrathin films are advantageous over interfaces because information about the electronic structure and local density of states can be directly obtained by using angle-resolved photoemission and scanning tunneling spectroscopy, respectively.

SrNbO$_3$ (SNO) has the same perovskite-type structure as STO but with a heavier transition metal Nb and a $4d^1$ electronic configuration for niobium, thus exhibiting metallic behavior. Bulk SNO is not stable under ambient conditions. Therefore, recently, SNO thin films were deposited on perovskite substrates *in vacuo* and have been intensively studied [20–22]. Since Sr(Ti$_{1-x}$Nb$_x$)O$_3$ ($x = 0.02-0.2$) showed a systematic enhancement in the SOC strength with increasing Nb concentration [23,24], SNO is a potential candidate for a Rashba interface with a high α_R. However, two important issues must be addressed: one issue is that SNO films on semiconductor STO or KTO substrates could show parallel conduction between the SNO film and an oxide-deficient surface of the substrate. Since the doped substrate surface shows high mobility at low temperature (T), it is difficult to separate the intrinsic SNO and the substrate contributions. Another issue is that the study on Sr(Ti$_{1-x}$Nb$_x$)O$_3$ assumed a D'Yakonov-Perel (DP)-type spin relaxation mechanism to estimate α_R [24], but there are other possible spin relaxation mechanisms. Thus, we must confirm that the DP-type mechanism dominates the spin relaxation in the SNO film.

Three types of spin relaxation mechanisms have been found for conductive electrons: Elliot-Yafet (EY) type, DP type, and Bir-Aronov-Pikus (BAP) type [25]. The EY mechanism describes the spin inversion caused by the momentum scattering of an electron from impurities and phonons. This spin inversion originates from an entanglement of spin-up and spin-down states caused by the SOC of lattice ions. Therefore, the spin relaxation time (τ_{so}) is proportional to the momentum scattering time (τ_p). The DP mechanism originates from spin precession processes with elastic scattering events. Rashba SOC lifts the spin degeneracy, and then spin-up and spin-down bands have different energies. This is equivalent to having a momentum-dependent internal magnetic field, by which spin processes occur. Momentum scattering causes fluctuations in the internal magnetic field and interrupts spin precession. Therefore, τ_{so} is inversely proportional to τ_p, in contrast to the behavior of the EY mechanism. The BAP mechanism originates from an electron-hole exchange interaction, while SNO is a d^1 metal and only has electrons on the Fermi surface. Thus, this mechanism can be disregarded for SNO films.

In this study, we examine the spin relaxation mechanism of SNO ultrathin films deposited on an insulator substrate. From the analysis of the magnetoresistance (MR) with weak antilocalization (WAL) theory for a series of films with different thicknesses (t) and disorders, we find that τ_{so} is inversely

*Corresponding author: hikaruokuma613@g.ecc.u-tokyo.ac.jp

proportional to τ_p, indicating DP-type spin relaxation and a dominant Rashba effect. The values of α_R are on the order of 1×10^{-12} eV m, which are larger than the values reported for other ultrathin films of metallic oxides.

II. EXPERIMENT

The SNO thin films are fabricated on the insulator (001)-oriented $(LaAlO_3)_{0.3}(Sr_2AlTaO_6)_{0.7}$ (LSAT) substrate by a pulsed laser deposition method *in vacuo* with a back pressure of 10^{-7} Torr at $900\,°C$. A ceramic target composed of $Sr_2Nb_2O_7$ is ablated by a KrF excimer laser ($\lambda = 248$ nm) with a repetition rate of 5 Hz and an energy fluence of $0.93-1.14\,J/cm^2$. The crystal structures of SNO (001) thin films are examined by an out-of-plane $2\theta/\omega$ scan and reciprocal space mapping with x-ray diffraction (Rigaku, Smart Lab). The film thicknesses of thicker films are directly measured by a surface profiler (Bruker, Dektak XT). It turns out that the measured film thickness is almost proportional to the deposition time for half a year when we deposited all SNO films listed in this paper. Therefore, the thicknesses of thinner films can be estimated with the deposition time. A detailed method is described in the Supplemental Material, Sec. A [26]. The surface uniformity is estimated with an atomic force microscope (AFM). Six aluminum wires were ultrasonically bonded on a bar-shaped sample, working as current and voltage probes. Ohmic contacts were confirmed down to the lowest temperature. The transport properties are examined by four-terminal resistance and Hall resistance measurements with these probes in a Physical Properties Measurement System (Quantum Design, PPMS) from 2 to 300 K and -7 to 7 T. Resistivities $\rho_{xx}(= R_{xx}\frac{wt}{l})$ were obtained from the measured resistance R_{xx} by a four-terminal configuration, where the width w of the rectangular film, the distance between voltage electrodes l, and the film thickness t were directly measured. We have checked for selected films that resistivities for the films with strip-shaped current electrodes were changed by 30% from the original measurement. In addition, the resistivity also slightly varied with different voltage electrodes on an identical sample, indicating that the resistivity exhibits weak variations in response to the inhomogeneous disorder at different locations in sample. To check the uniformity of the sample, we also measured the resistivities for selected films using a van der Pauw method and found that they are at most smaller by 10% than the values measured by the four-terminal method with original electrodes. The variation of resistivity in the sample is smaller than the changes in resistivity resulting from disorder between different samples. For more detailed explanation, see the Supplemental Material, Sec. B [26]. Pulsed laser deposition (PLD) is known not to be very reproducible between different sample growths, in contrast to molecular beam epitaxy, while our PLD method shows a good reproducibility with respect to the film thickness, as seen in Fig. S1 in the Supplemental Material, Sec. A [26]. The band structure and Fermi surfaces of SNO are calculated by the density functional theory (DFT) [27,28]. The electrical conductivity components are calculated by BoltzTrap code with the semiclassical Boltzmann transport equation on the band structure [29]. Detailed information can be found in the Supplemental Material, Sec. C [26].

III. RESULTS AND DISCUSSION

Figure 1(a) shows an out-of-plane $2\theta/\omega$ scan of the SNO films on the LSAT substrates (SNO/LSAT) ($a = 0.3868$ nm) with t ranging 3.4–8.7 nm. Figure 1(b) shows an out-of-plane lattice constant with various t between 3.4 and 48.0 nm. The out-of-plane lattice constant ranged 4.038–4.100 Å, which was always larger than the lattice constant in a pseudocubic approximation ($a = 4.023$ Å) [30] and is in agreement with a previous report on a SNO film [20]. A reciprocal space mapping (RSM) was performed on a (103) reflection of SNO/LSAT with $t = 48.0$ nm, as shown in Fig. 1(c). The in-plane and out-of-plane lattice constants were obtained as 3.980 and 4.073 Å, respectively. The cell volume of the SNO film was smaller than that of bulk SNO by approximately 1%, probably indicating small off-stoichiometry variations for the film. The smaller in-plane lattice constant indicates that the film was partly strained by the substrate. Figure 1(d) shows the rocking curve of the SNO (002) reflection peak of SNO/LSAT with $t = 7.4$ nm. The full width at half maximum is $0.16°$, indicating high crystalline quality. Figure 1(e) displays the surface morphology of SNO/LSAT with $t = 6.9$ nm obtained by AFM. The root mean square (rms) roughnesses of SNO/LSAT with t ranging 3.4–8.7 nm were always less than 1 nm, indicating that the SNO films had flat surfaces.

We examined the temperature dependence of the transport properties of SNO/LSAT films with various t values. Figure 2(a) shows the longitudinal resistivity (ρ_{xx}) of the films shown in Fig. 1(a). We observed a metal-to-insulator (or bad metal) transition (MIT) of the SNO films by reducing t. Films thicker than 4.1 nm exhibited metallic behavior with a resistivity minimum at a certain temperature T_{min}, which increased with decreasing t. In contrast, the films with $t \leqslant 4.1$ nm exhibited insulating (or bad metal) behavior over the entire temperature range. For all films, the origin of the resistivity increase on cooling was well explained by electron-electron interaction (EEI) and quantum interference effects. A detailed discussion can be found in the Supplemental Material, Sec. D [26] (see also Ref. [31] therein). The film with $t = 4.1$ nm is more insulating than the films with $t = 3.4$ and 3.7 nm, and the film with $t = 6.9$ nm is more metallic than the films with $t = 7.2$ and 8.7 nm. These behaviors suggest that the disorder effects in the film with $t = 4.1$ nm (6.9 nm) are larger (smaller) than those in films with $t = 3.4$ and 3.7 nm (7.2 and 8.7 nm). Similar behavior is seen in $SrVO_3$ ultrathin films [32]. Figure 2(b) shows the Hall data for films with t ranging 3.7–14.9 nm. The negative linear Hall resistances are observed for all films, indicating the single electron band. We obtained the carrier density (n) from the Hall data and the mobility (μ) from ρ and n. In Fig. 2(c), we plotted ρ_{xx}, n, and μ at 10 K (denoted as ρ_{xx10K}, n_{10K}, and μ_{10K}, respectively) for the films shown in Fig. 2(a) and others not shown in Fig. 2(a), which are indicated by solid and open symbols, respectively, against t ranging 3.4–11.2 nm. ρ_{xx10K} increased by nearly two orders of magnitude with decreasing t, while both n_{10K} and μ_{10K} decreased by nearly one order of magnitude with decreasing t. These results indicate that both an increase in disorder and a decrease in carrier density are responsible for the insulating behavior of the thinner films with $t \leqslant 4.1$ nm.
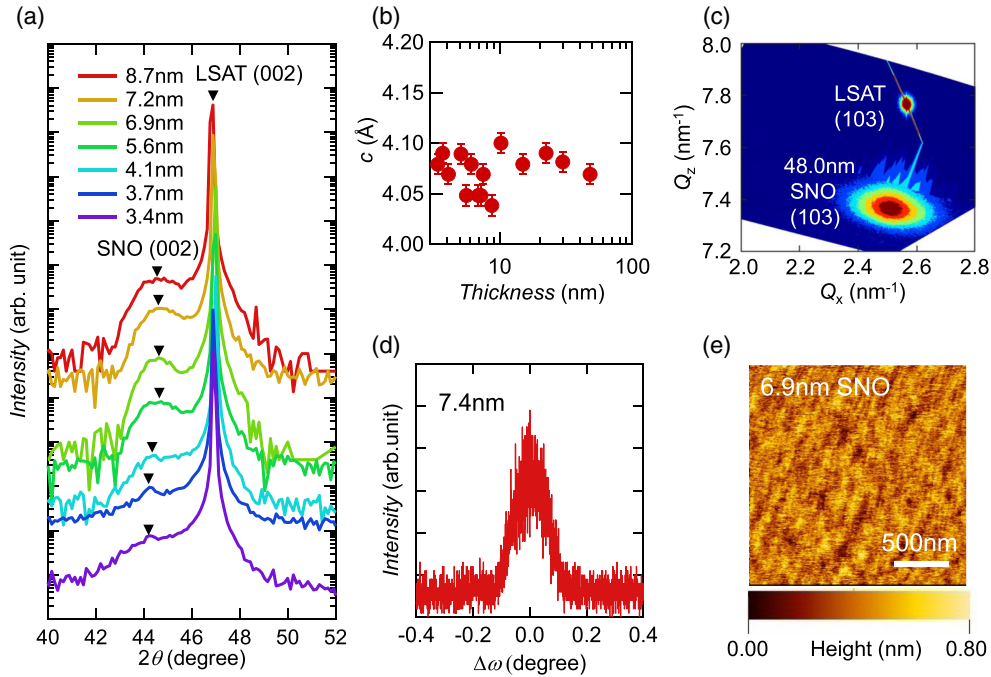
FIG. 1. (a) Out-of-plane $2\theta/\omega$ scan of representative SNO/LSAT with various t values ranging 3.4–8.7 nm. (b) Out-of-plane lattice constant versus t plots. (c) Reciprocal space mapping on a (103) reflection of SNO/LSAT with $t = 48.0$ nm. (d) Rocking curve of the SNO (002) peak of SNO/LSAT with $t = 7.4$ nm. (e) AFM surface morphology of SNO/LSAT with $t = 6.9$ nm.

Moreover, we noticed the scattering of the data points of ρ_{xx10K}, n_{10K}, and μ_{10K} in proximity to the individual lines drawn as visual references. This is probably due to the difference in the disorder of the films with a given thickness, such as disorder originating from oxygen vacancies, defects, and surface degradation. Although the as-deposited samples were fabricated with the same deposition temperature and pressure,

the laser energy and the target condition in our experiment were inevitably changed between depositions. In addition, room temperature and humidity also differed between depositions. We think that these different conditions induce changes in oxygen vacancies, defects, and surface degradations in the as-deposited samples. Indeed, a change from MIT owing to surface degradation was reported for various oxide thin films
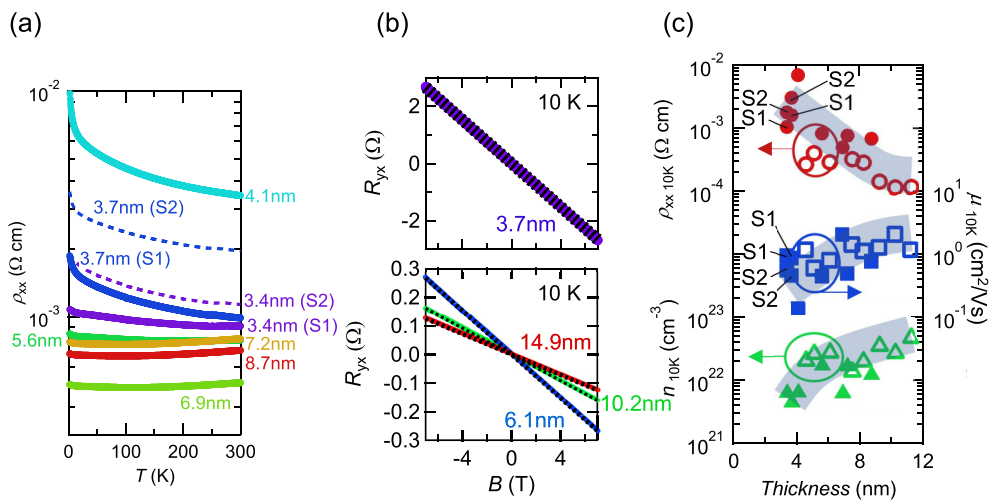
FIG. 2. (a) Temperature dependence of the longitudinal resistivity (ρ_{xx}) for films with various t values ranging 3.4–8.7 nm. For 3.4 and 3.7 nm, the different areas in the same sample are named S1 and S2. (b) Hall resistance versus magnetic field for films with t ranging 3.7–14.9 nm. (c) ρ_{xx}, carrier density (n), and mobility (μ) at 10 K (ρ_{xx10K}, n_{10K}, and μ_{10K}) plotted against t for films with t ranging 3.4–11.2 nm. Solid and open symbols correspond to the data for the films indicated in (a) and others not shown in (a), respectively. The gray bold lines are provided as guides for the eye.
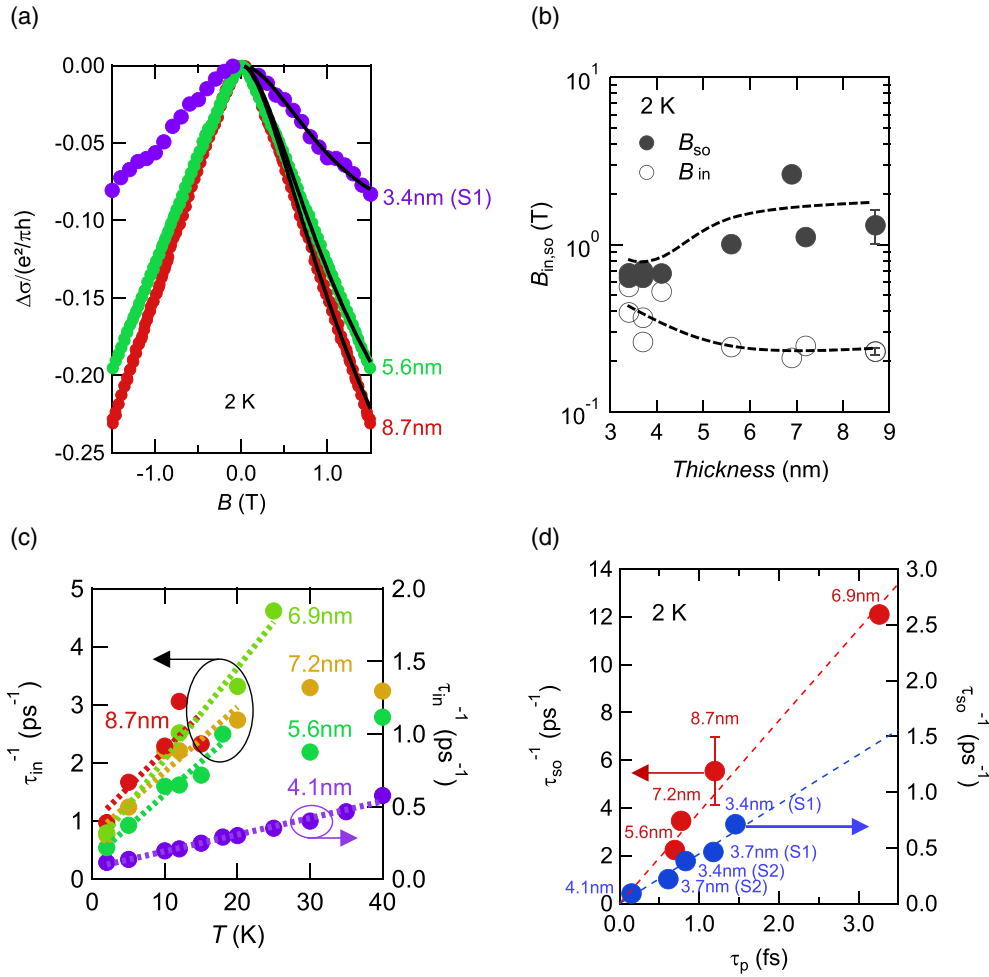
FIG. 3. (a) $\Delta\sigma = \sigma(B) - \sigma(0)$ in units of $e^2/\pi h$ measured in the perpendicular magnetic field for films with $t = 3.4$ nm (S1), 5.6 nm, and 8.7 nm at 2 K. The black solid lines are fits to the data based on ILP theory [Eq. (4)]. (b) Effective fields B_{in} and B_{so} extracted from the fits of MR at 2 K to Eq. (4) plotted against t. (c) Inverse of the inelastic scattering time (τ_{in}^{-1}) at 2 K for the films with t ranging 4.1–8.7 nm as a function of T. The dotted straight lines represent the linear fits. (d) Inverse of the spin relaxation time (τ_{so}^{-1}) versus the momentum scattering time (τ_p) at 2 K for the films with t ranging 5.6–8.7 nm and 3.4–4.1 nm. The dashed lines are fits of the data to $\tau_{so}^{-1} \propto \tau_p$. The linear relation $\tau_{so}^{-1} \propto \tau_p$ clearly indicates that the DP spin relaxation mechanism is dominant in the SNO films rather than the EY spin relaxation mechanism, which follows $\tau_{so} \propto \tau_p$.

with a fixed thickness by the absence of the surface capping layer [32–35].

To estimate the SOC strength, we measured ρ for the films shown in Fig. 1(a) as a function of a perpendicular magnetic field (B) at 2 K. The data for several films and all films are shown in the form of a magnetoconductance $\Delta\sigma(B)[\equiv \sigma(B) - \sigma(0)]$ in Fig. 3(a) and the Supplemental Material, Sec. E [26], respectively, where σ denotes the inverse of the sheet resistance $R_{xx}\frac{w}{l}$. All films showed a positive MR, which originates from two contributions in the weakly disordered systems: WAL and EEI. At high B, the latter contribution is dominant, and thus it is inappropriate to estimate SOC by WAL theory. On the other hand, EEI contribution is negligible at low B, and $\Delta\sigma(B)$ was well reproduced by WAL. A detailed discussion is found in the Supplemental Material, Sec. F [26] (see also Refs. [36–40] therein). We fitted $\Delta\sigma(B)$ both with Hikami-Larkin-Nagaoka (HLN) theory taking the EY spin-relaxation mechanism into account, and Iordanskii-Lyanda-Pikus (ILP) theory taking the DP spin-

relaxation mechanism into account. In HLN theory, MR is described by the following equation [41,42]:

$$\frac{\Delta\sigma(B)}{\sigma_0} = -\left[\Psi\left(\frac{1}{2} + \frac{(\hbar/4eL_p^2)}{B}\right) - \ln\left(\frac{\hbar/4eL_p^2}{B}\right)\right.$$

$$\left. - \Psi\left(\frac{1}{2} + \frac{B_{in} + B_{so}}{B}\right) + \ln\frac{B_{in} + B_{so}}{B}\right], \quad (1)$$

$$L_p = \frac{\hbar k_F \mu}{e}, \quad (2)$$

$$k_F = \sqrt{2n_s\pi}, \quad (3)$$

where $\sigma_0 = e^2/\pi h$, e is the elementary charge, Ψ is the digamma function, h and $\hbar$ are the Planck constant and Dirac's constant, respectively, L_p is the momentum scattering length, B_{in} and B_{so} are effective fields related to inelastic and spin-orbit scattering, respectively (for details, see below), k_F is the Fermi wave number, and n_s is the sheet carrier density. As shown in Fig. S7 in the Supplemental Material, Sec. G [26],

$\Delta\sigma(B)$ at 2 K for films with $t = 3.4$ and 4.1 nm followed Eq. (1); however, the values of L_p extracted from the fitting were nearly two orders of magnitude larger than those obtained from k_F and μ, which are shown in the Supplemental Material, Sec. H [26]. Therefore, it is unlikely that the B dependence of the MR is explained by HLN theory taking the EY spin-relaxation mechanism into account. A detailed discussion is found in the Supplemental Material, Sec. G [26].

Next, we focus on ILP theory, which describes the MR with the following equation [43,44]:

$$\frac{\Delta\sigma(B)}{\sigma_0}$$
$$= -\left[\frac{1}{2}\Psi\left(\frac{1}{2} + \frac{B_{in}}{B}\right) - \frac{1}{2}\ln\frac{B_{in}}{B} - \Psi\left(\frac{1}{2} + \frac{B_{in} + B_{so}}{B}\right)\right.$$
$$+ \ln\frac{B_{in} + B_{so}}{B} - \frac{1}{2}\Psi\left(\frac{1}{2} + \frac{B_{in} + 2B_{so}}{B}\right)$$
$$\left. + \frac{1}{2}\ln\frac{B_{in} + 2B_{so}}{B}\right]. \tag{4}$$

This equation describes the single-band WAL effect, which is insufficient for a multiband system [45,46]. However, experimental evidence of the multiband effect is not observed both in the Hall measurement [as shown in Fig. 2(b)] and the magnetoconductance analysis (a detailed discussion is given in Fig. S9 in the Supplemental Material, Sec. I [26]). Therefore, ILP theory can be applied for the fitting analysis. As shown in Fig. 3(a), $\Delta\sigma(B)$ at 2 K followed Eq. (4). Figure 3(b) shows the t dependence of B_{in} and B_{so} deduced from the fitting by Eq. (4). Here, B_{in} and B_{so} are defined as values when the error between data and fitting is minimum. For 8.7-nm-thick SNO film, for example, the error bar of B_{so} is obtained from the errors versus B_{so} plots shown in Fig, S11(b) in the Supplemental Material, Sec. J, to be 0.3 T, which is smaller than the optimum value of $B_{so} = 1.3$ T. For more detailed information, see the Supplemental Material, Sec. J [26]. It was found that B_{so} was always larger than B_{in}, indicating that spin-orbit scattering was dominant over inelastic scattering. With a decrease in t to 5.6 nm, B_{so} decreased gradually, while B_{in} remained nearly constant. With a further decrease in t, B_{in} increased and was comparable to B_{so} for $t \leqslant 4.1$ nm. This result implies that inelastic scattering was enhanced as the system entered the insulating (bad metal) regime, and then the contribution of inelastic scattering was comparable to that of spin-orbit scattering.

Then, we examined the three characteristic times [inelastic scattering time (τ_{in}), τ_{so}, and τ_p] for the SNO films. B_{in} and B_{so} are related to an inelastic scattering length (time) L_{in} (τ_{in}) and a spin-orbit scattering length (time) L_{so} (τ_{so}), respectively, with the following equations:

$$B_{in,so} = \frac{\hbar}{4eL_{in,so}^2}, \tag{5}$$

$$L_{in,so} = \sqrt{D\tau_{in,so}}, \tag{6}$$

$$D = \frac{1}{2}v_F^2\tau_p, \tag{7}$$

$$\tau_p = \frac{\mu m}{e}, \tag{8}$$

where D is the diffusion constant, v_F is the Fermi velocity, and m is the effective mass. We employed $m = 2.76m_0$ [21] for all films, where m_0 is the free electron mass. Figure 3(c) displays the inverse of the inelastic scattering time (τ_{in}^{-1}) as a function of T for various films. The linear relation between τ_{in}^{-1} and T was observed and was well explained assuming that electron-electron scattering was dominant [47,48].

Figure 3(d) shows τ_{so}^{-1} as a function of τ_p for films with $t \geqslant 5.6$ nm (metallic films, red solid circles) and those with $t \leqslant 4.1$ nm (insulating films, blue solid circles). For both the metallic and insulating films, τ_{so}^{-1} was proportional to τ_p, verifying that the main spin relaxation mechanism was DP-type spin relaxation ($\tau_{so} \propto \tau_p^{-1}$) instead of EY-type spin relaxation ($\tau_{so} \propto \tau_p$). Note that the slope of the red dashed line for the metallic films is larger than that of the blue dashed line for the insulating films. The abrupt decrease in τ_{so}^{-1} near MIT was also reported in ultrathin SIO films with the sheet resistance $R_s = 3-4$ kΩ below quantum resistance $R_Q = 25$ kΩ, while τ_{so} was governed by the EY mechanism for the SIO films [49]. For SNO, the R_s of films with $t = 3.4-4.1$ nm ranged 3–25 kΩ, and L_p ranged 0.12–0.75 nm, which are close to the value of the lattice constant. Therefore, one explanation for the sudden reduction of τ_{so}^{-1} is a change in the band structure at the MIT. According to the DP spin relaxation mechanism, the relation between τ_{so}^{-1} and τ_p is expressed as [19,44,50–52]

$$\tau_{so}^{-1} = \frac{1}{2}\left(\frac{\Delta_{so}}{\hbar}\right)^2\tau_p, \tag{9}$$

where Δ_{so} is the energy band splitting due to SOC. Δ_{so} was estimated with Eq. (9) and plotted against t in Fig. 4(a). Thus, the reduction in τ_{so}^{-1} is related to the decrease in Δ_{so} by a factor of approximately 3 at the MIT. The values of Δ_{so} for our SNO ultrathin films were largest among those reported for other oxide materials.

Figure 4(b) shows α_R at 2 K as a function of t. In the metallic regime, Δ_{so} is related to k_F and α_R with the following expression by assuming a parabolic band structure and the single spin winding in the spin texture:

$$\Delta_{so} = 2k_F\alpha_R, \tag{10}$$

We could not determine whether single or triple spin winding is dominant in the spin texture. A detailed discussion can be found in the Supplemental Material, Sec. I [26]. We employed k_F calculated from Eq. (3) using an experimental value of n_s, and obtained α_R from Eq. (10) for films of all thicknesses, although k_F is not a good parameter in the insulator regime. Thus, α_R for films with $t \leqslant 4.1$ nm is not a very reliable value. The values of α_R for our SNO ultrathin films for all thicknesses were larger than those reported for other ultrathin films of metallic oxides, SrIrO$_3$ (SIO) (green solid squares) and La$_{2/3}$Sr$_{1/3}$MnO$_3$ (LSMO) (light blue solid triangles), and comparable to or smaller than the values reported for oxide heterointerfaces [13–16], which are on the order of $10^{-12}-10^{-11}$ eV m. To obtain α_R, different research groups used different methods of resistivity measurements. We deduced α_R for the same sample from the measurements using a four-terminal method with pointlike and Hall-bar contacts, and the van der Pauw method. The difference of the measurement method slightly changed the value of α_R but did not alter the conclusion that the values of α_R in
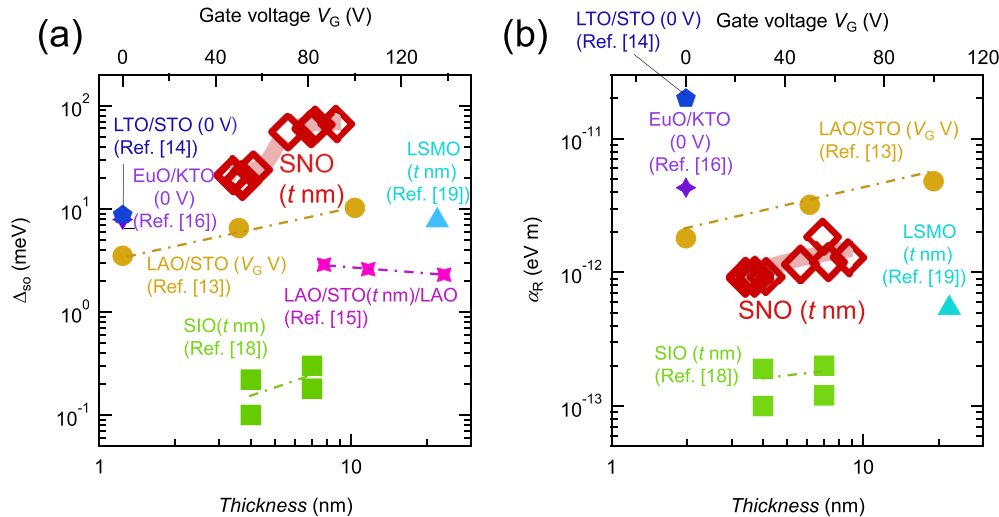
FIG. 4. (a) Energy band splitting due to SOC (Δ_{so}) for oxide materials of metallic films, SNO/LSAT (this study), SIO/STO [18], LSMO/STO [19] versus t (bottom axis) and interface heterostructures, LaAlO$_3$(LAO)/STO [13], LaTiO$_3$(LTO)/STO [14], LAO/STO/LAO [15], EuO/KTO [16] versus gate voltage (top axis). (b) Rashba parameter (α_R) for the oxide materials.

SNO/LSAT are largest among the values reported for other ultrathin films of metallic oxides. A more detailed discussion is given in the Supplemental Material, Sec. K [26]. It is expected that α_R can be enhanced by reducing the film thickness, while the MIT at the ultrathin film prevents us from seeing this enhancement. Therefore, we expect that, combined with improved fabrication and a sophisticated carrier doping technique, SNO metallic ultrathin films with a few monolayers will be a promising material system for practical applications in Rashba-based spintronics devices.

IV. CONCLUSION

In summary, to reveal the spin relaxation mechanism of SNO ultrathin films, the transport properties of a series of films with different t were measured on both sides of the MIT. The MR at 2 K for the films with various t and disorder was analyzed using WAL theory, and it was found that $\tau_{so} \propto \tau_p^{-1}$. This result verified the DP-type spin relaxation mechanism, indicating the dominant Rashba effect. The values of α_R were on the order of 1×10^{-12} eV m, which were largest in the values reported for other ultrathin films of metallic oxides.

[1] E. I. Rashba, Sov. Phys. Solid State **2**, 1109 (1960).

[2] Y. A. Bychkov and E. I. Rashba, J. Phys. C **17**, 6039 (1984).

[3] R. Winkler, *Spin-Orbit Coupling Effects in Two-dimensional Electron and Hole Systems*, Springer Tracts in Modern Physics Vol. 191 (Springer, Berlin, 2003).

[4] A. Manchon, H. C. Koo, J. Nitta, S. M. Frolov, and R. Duine, Nat. Mater. **14**, 871 (2015).

[5] A. Soumyanarayanan, N. Reyren, A. Fert, and C. Panagopoulos, Nature (London) **539**, 509 (2016).

[6] J. Sinova, D. Culcer, Q. Niu, N. A. Sinitsyn, T. Jungwirth, and A. H. MacDonald, Phys. Rev. Lett. **92**, 126603 (2004).

[7] S. Datta and B. Das, Appl. Phys. Lett. **56**, 665 (1990).

[8] H. C. Koo, J. H. Kwon, J. Eom, J. Chang, S. H. Han, and M. Johnson, Science **325**, 1515 (2009).

[9] E. Lesne, Yu Fu, S. Oyarzun, J. C. Rojas-Sánchez, D. C. Vaz, H. Naganuma, G. Sicoli, J.-P. Attané, M. Jamet, E. Jacquet, J.-M. George, A. Barthélémy, H. Jaffrès, A. Fert, M. Bibes, and L. Vila, Nat. Mater. **15**, 1261 (2016).

[10] J. C. Rojas Sánchez, L. Vila, G. Desfonds, S. Gambarelli, J. P. Attané, J. M. De Teresa, C. Magén, and A. Fert, Nat. Commun. **4**, 2944 (2013).

[11] J.-C. Rojas-Sánchez, S. Oyarzún, Y. Fu, A. Marty, C. Vergnaud, S. Gambarelli, L. Vila, M. Jamet, Y. Ohtsubo, A. Taleb-Ibrahimi, P. Le F'evre, F. Bertran, N. Reyren, J.-M. George, and A. Fert, Phys. Rev. Lett. **116**, 096602 (2016).

[12] J. Sinova, S. O. Valenzuela, J. Wunderlich, C. H. Back, and T. Jungwirth, Rev. Mod. Phys. **87**, 1213 (2015).

[13] A. D. Caviglia, M. Gabay, S. Gariglio, N. Reyren, C. Cancellieri, and J. M. Triscone, Phys. Rev. Lett. **104**, 126803 (2010).

[14] M. J. Veit, R. Arras, B. J. Ramshaw, R. Pentcheva, and Y. Suzuki, Nat. Commun **9**, 1458 (2018).

[15] W. Lin, L. Li, F. Dogan, C. Li, H. Rotella, X. Yu, B. Zhang, Y. Li, W. S. Lew, S. Wang, W. Prellier, S. J. Pennycook, J. Chen, Z. Zhong, A. Manchon, and T. Wu, Nat. Commun. **10**, 3052 (2019).

[16] N. Kumar, N. Wadehra, R. Tomar, S. Kumar Shama, Y. Singh, S. Dattagupta, and S. Chakraverty, Adv. Quantum Technol. **4**, 2000081 (2021).

[17] N. Wadehra, R. Tomar, R. M. Varma, R. K. Gopal, Y. Singh, S. Dattagupta, and S. Chakraverty, Nat. Commun. **11**, 874 (2020).

[18] L. Zhang, Y. B. Chen, B. Zhang, J. Zhou, S. Zhang, Z. Gu, S. Yao, and Y. F. Chen, J. Phys. Soc. Jpn. **83**, 054707 (2014).

[19] S. P. Chiu, M. Yamanouchi, T. Oyamada, H. Ohta, and J. J. Lin, Phys. Rev. B **96**, 085143 (2017).

[20] D. Oka, Y. Hirose, S. Nakano, T. Fukumura, and T. Hasegawa, Phys. Rev. B **92**, 205102 (2015).

[21] Y. Park, D. Oka, Y. Hirose, T. Hasegawa, A. Paul, A. Pogrebnyakov, V. Gopalan, T. Birol, and R. Engel-Herbert, Commun. Phys. **3**, 102 (2020).

[22] J. M. Ok, N. Mohanta, J. Zhang, S. Yoon, S. Okamoto, E. S. Choi, H. Zhou, M. Briggeman, P. Irvin, A. R. Lupini, Y. Y. Pai, E. Skoropata, C. Sohn, H. Li, H. Miao, B. Lawrie, W. S. Choi, G. Eres, J. Levy, and H. N. Lee, Sci. Adv. **7**, eabf9631 (2021).

[23] H. Jin, K. Lee, S.-H. Baek, J.-S. Kim, B. Cheong, B. H. Park, S. Yoon, B. J. Suh, C. Kim, S. S. A. Seo, and S. Lee, Sci. Rep. **6**, 34295 (2016).

[24] S. W. Cho, M. Lee, S. Woo, K. Yim, S. Han, W. S. Choi, and S. Lee, Sci. Rep. **8**, 5739 (2018).

[25] J. Fabian and S. D. Sarma, J. Vac. Sci. Technol. B **17**, 1708 (1999).

[26] See Supplemental Material at http://link.aps.org/supplemental/10.1103/PhysRevMaterials.8.015001 for thickness estimation, resistivities measured using different methods, transport properties of SNO predicted by band calculation, origin of the resistivity increase at low temperature, fitting to ILP theory taking the DP spin-relaxation mechanism into account, magnetic field range of weak antilocalization, fitting to HLN theory taking the EY spin-relaxation mechanism into account, film thickness dependence of the momentum scattering length, fitting of the magnetoconductance by ILP (single-band) and multiband model, estimation of error bar for the ILP fitting, and Rashba parameter for oxide materials and methods of resistivity measurements.

[27] P. Giannozzi, S. Baroni, N. Bonini, M. Calandra, R. Car, C. Cavazzoni, D. Ceresoli, G. L. Chiarotti, M. Cococcioni, I. Dabo, A. D. Corso, S. de Gironcoli, S. Fabris, G. Fratesi, R. Gebauer, U. Gerstmann *et al.*, J. Phys.: Condens. Matter **21**, 395502 (2009).

[28] P. Giannozzi, O. Andreussi, T. Brumme, O. Bunau, M. B. Nardelli, M. Calandra, R. Car, C. Cavazzoni, D. Ceresoli, M. Cococcioni, N. Colonna, I. Carnimeo, A. D. Corso, S. de Gironcoli, P. Delugas *et al.*, J. Phys.: Condens. Matter **29**, 465901 (2017).

[29] G. Madsen and D. J. Singh, Comput. Phys. Commun. **175**, 67 (2006).

[30] R. B. Macquart, B. J. Kennedy, and M. Avdeev, J. Solid State Chem. **183**, 2400 (2010).

[31] H.-Z. Lu and S.-Q. Shen, Phys. Rev. Lett. **112**, 146601 (2014).

[32] H. Okuma, Y. Katayama, K. Otomo, and K. Ueno, Phys. Rev. B **105**, 045138 (2022).

[33] Z. Liao, F. Li, P. Gao, L. Li, J. Guo, X. Pan, R. Jin, E. W. Plummer, and J. Zhang, Phys. Rev. B **92**, 125123 (2015).

[34] D. J. Groenendijk, N. Manca, G. Mattoni, L. Kootstra, S. Gariglio, Y. Huang, E. van Heumen, and A. D. Caviglia, Appl. Phys. Lett. **109**, 041906 (2016).

[35] G. Wang, Z. Wang, M. Meng, M. Saghayezhian, L. Chen, C. Chen, H. Guo, Y. Zhu, E. W. Plummer, and J. Zhang, Phys. Rev. B **100**, 155114 (2019).

[36] J. Ryu, M. Kohda, and J. Nitta, Phys. Rev. Lett. **116**, 256802 (2016).

[37] P. A. Lee and T. V. Ramakrishnan, Phys. Rev. B **26**, 4009 (1982).

[38] P. A. Lee and T. V. Ramakrishnan, Rev. Mod. Phys. **57**, 287 (1985).

[39] M. A. Howson and D. Greig, J. Phys. F: Met. Phys. **13**, L155 (1983).

[40] C. Li, M. Boubeche, L. Zeng, Y. Ji, Q. Li, D. Guo, Q. Zhu, D. Zhong, H. Luo, and H. Wang, Phys. Status Solidi RRL **16**, 2100650 (2022).

[41] S. Hikami, A. I. Larkin, and Y. Nagaoka, Prog. Theor. Phys. **63**, 707 (1980).

[42] S. X. Zhang, R. D. McDonald, A. Shekhter, Z. X. Bi, Y. Li, Q. X. Jia, and S. T. Picraux, Appl. Phys. Lett. **101**, 202403 (2012).

[43] S. V. Iordanskii, Y. B. Lyanda-Geller, and G. E. Pikus, JETP Lett. **60**, 206 (1994).

[44] W. Knap, C. Skierbiszewski, A. Zduniak, E. Litwin-Staszewska, D. Bertho, F. Kobbi, J. L. Robert, G. E. Pikus, F. G. Pikus, S. V. Iordanskii, V. Mosser, K. Zekentes, and Yu. B. Lyanda-Geller, Phys. Rev. B **53**, 3912 (1996).

[45] P. Seiler, E. Lettl, D. Braak, and T. Kopp, Phys. Rev. B **100**, 121404(R) (2019).

[46] P. Seiler, E. Lettl, D. Braak, and T. Kopp, Phys. Rev. B **100**, 115415 (2019).

[47] B. L. Altshuler, A. G. Aronov, and D. E. Khmelnitsky, J. Phys. C **15**, 7367 (1982).

[48] S. Chakravarty and A. Schmid, Phys. Rep. **140**, 193 (1986).

[49] L. Zhang, X. Jiang, X. Xu, and X. Hong, APL Mater. **8**, 051108 (2020).

[50] M. I. D'Yakonov and V. I. Perel', Sov. J. Exp. Theor. Phys. **33**, 1053 (1971).

[51] T. Koga, J. Nitta, T. Akazaki, and H. Takayanagi, Phys. Rev. Lett. **89**, 046801 (2002).

[52] C. Schierholz, T. Matsuyama, U. Merkt, and G. Meier, Phys. Rev. B **70**, 233311 (2004).